$\rho - \omega$ interference in $\bar{p}p \to \pi^+\pi^-\eta$ at rest

Andreas Ehmanns

Institut für Strahlen– und Kernphysik, Universität Bonn, D–53115 Bonn, Germany

Contents

Chapter 1

1.1 Preselection

The data for the analysis of the $\pi^+\pi^-\eta$ final state in liquid hydrogen have been taken in three run periods with a special 2-prong trigger. The following cuts were applied on data in a first selection step (golden tracks and golden γ's):

GOLDEN TRACKS

- First hit layer 1 - 3
- Last hit layer 20 - 23
- More than 15 hits
- Track quality < 10

GOLDEN GAMMAS

- E1/E9 < 0.96
- no TAXI-Flag
- no DOLBY-C-Flag
- ECLUBC=14 MeV, EPEDBC=14 MeV, ECLSBC=13 MeV

In a second selection step additional cuts reduce the data sample according to Table 1.1.

- 2 charged tracks
- Reject PED's with central crystal of type 13 (outer ring of Barrel)
- Difference of charge < 0.1
- exactly 2γ

Since η and η' decay into 2 photons, we require two golden γ.
Table 1.1 gives a survey of the data reduction for the two-prong triggered data.

run period	June 1991	August 1991	June 1994	Σ
Successfull tracking	2101879	2542756	9661435	14306070
2 golden tracks	1746757	2058092	8459166	12264015
crystal type 13	1557128	1813856	7588448	10959432
charge conservation	1445297	1640060	6727186	9812543
2 photons	241655	295902	1226203	1763760

Table 1.1: The result of the first selection steps.

1.2 Kinematic fitting

After preselection the remaining data were fitted kinematically. For this purpose we used the standard program CBKFIT. Due to the fact that two photons are dominantly created trough decays of π^0, η and η' we fit the following hypotheses:

$$\begin{aligned} \bar{\mathrm{p}}\mathrm{p} &\rightarrow \pi^+\pi^-\gamma\gamma \quad (4\mathrm{C}) \\ \bar{\mathrm{p}}\mathrm{p} &\rightarrow \pi^+\pi^-\pi^0 \quad (5\mathrm{C}) \\ \bar{\mathrm{p}}\mathrm{p} &\rightarrow \pi^+\pi^-\eta \quad (5\mathrm{C}) \\ \bar{\mathrm{p}}\mathrm{p} &\rightarrow \pi^+\pi^-\eta' \quad (5\mathrm{C}) \end{aligned}$$

To distinguish between the $\pi^+\pi^-\pi^0$, the $\pi^+\pi^-\eta$ and the $\pi^+\pi^-\eta'$ final states we used the following cuts:

- successful fit of 2γ hypothesis
- $\mathrm{Cl}(\bar{\mathrm{p}}\mathrm{p} \rightarrow \pi^+\pi^-\pi^0) \geq 15\%$ for the $\pi^+\pi^-\pi^0$ final state
- $\mathrm{Cl}(\bar{\mathrm{p}}\mathrm{p} \rightarrow \pi^+\pi^-\eta) \geq 10\%$ for the $\pi^+\pi^-\eta$ final state
- $\mathrm{Cl}(\bar{\mathrm{p}}\mathrm{p} \rightarrow \pi^+\pi^-\eta') \geq 10\%$ and $\mathrm{Cl}(\bar{\mathrm{p}}\mathrm{p} \rightarrow \pi^+\pi^-\eta) \leq 10\%$ for the $\pi^+\pi^-\eta'$ final state

To achieve flat confidence level distributions (see Figure 1.2) and Gaussian shaped pulls several error scalings were tried for different run periods. In table 1.2 the scaling factors which were used are listed.

run period	$1/P_{xy}(\pi^+)$	$1/P_{xy}(\pi^-)$	$\Delta\alpha$	$\Delta\psi$	$\Delta\lambda$	Δ E	$\Delta\phi$	$\Delta\theta$
Jun '91	+1/18GeV	+1/30GeV	1	0.95	0.95	0.01	0.8	0.7
Aug '91	-1/70GeV	-1/60GeV	1.15	1.15	1	–	1	1
Jun '94	–	-1/58GeV	1.2	1.2	1.5	–	1	1

Table 1.2: Correction factors for the kinematic fit

Figure 1.1 shows the pulls for the nine kinematic quantities superimposed with Gaussian functions. They give a good description of the distribution with standard deviations and mean values are given in table 1.3.

	$\psi+$	$\psi-$	$1/P_{xy}+$	$1/P_{xy}-$	$\tan(\lambda)+$	$\tan(\lambda)-$	ϕ	θ	$\sqrt{E}$
$\bar{x}$	-0.06	-0.001	-0.002	0.03	-0.16	-0.16	0.08	-0.08	0.09
σ	1.09	1.10	1.08	1.12	1.06	1.07	0.98	1.03	1.10

Table 1.3: Mean and standard deviation of the pulls.

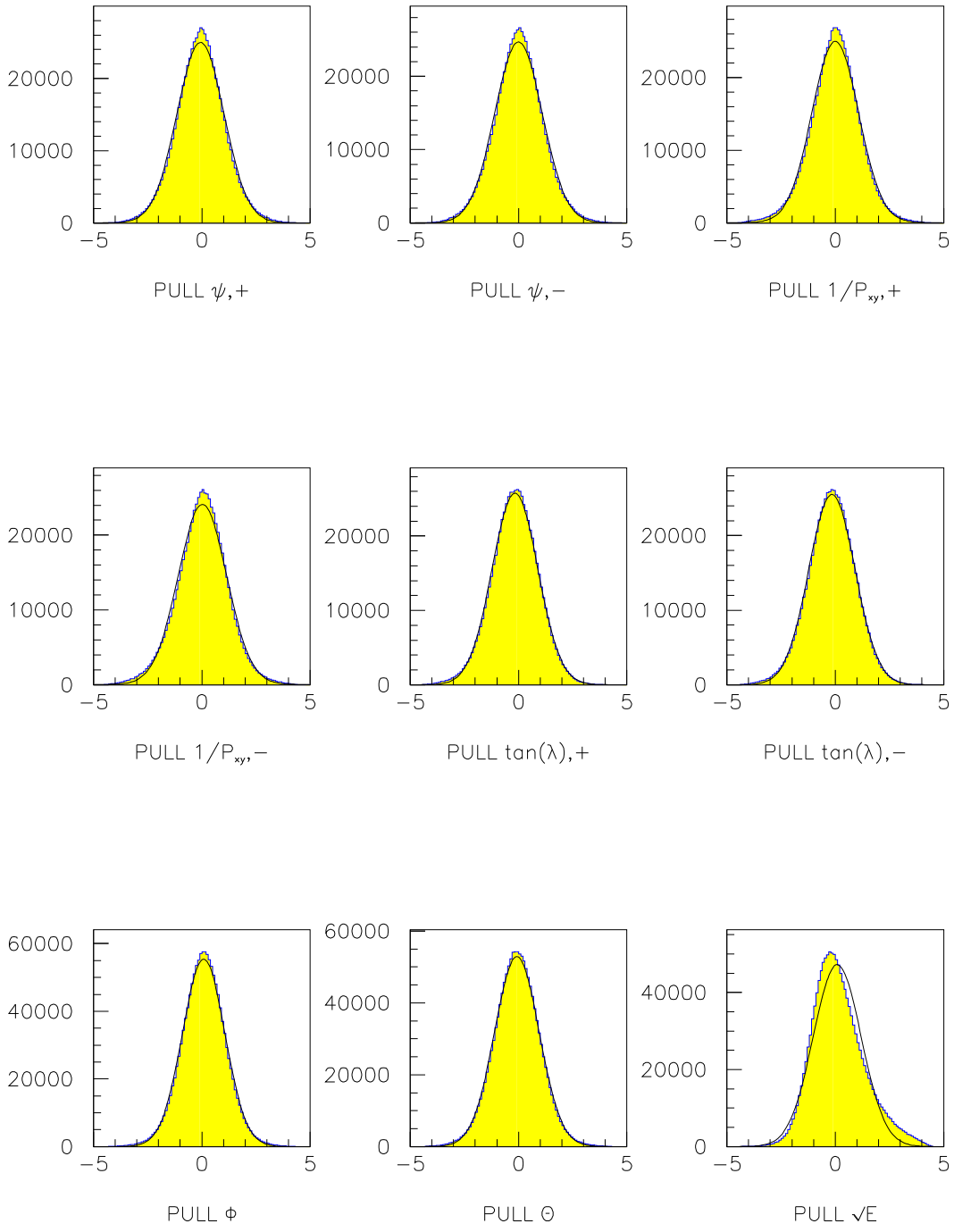

Figure 1.1: Distribution of the pulls for the nine kinematic quantities for 5C-fit $\pi^+\pi^-\pi^0$.

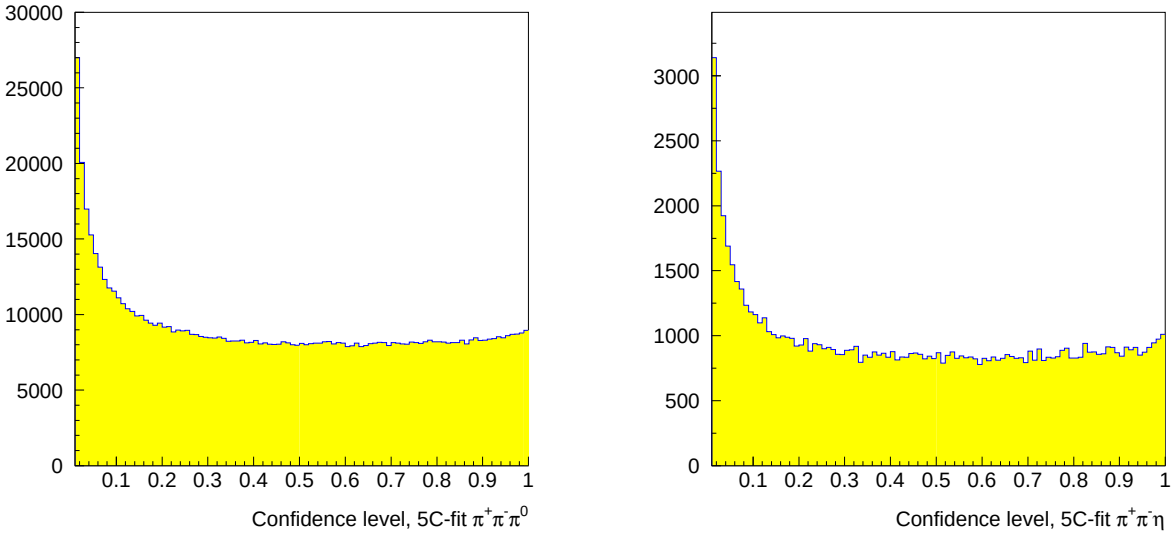

Figure 1.2: Confidence level distributions for $\pi^+\pi^-\pi^0$ and for $\pi^+\pi^-\eta$

The (fitted and non-fitted) $\gamma\gamma$ invariant mass spectrum is shown in figure 1.3. A clear signal for the decays $\pi^0 \to \gamma\gamma$ and $\eta \to \gamma\gamma$ is observed (Figure 1.3.a)). In Figure 1.3.b) the 2γ invariant mass is shown in the ω- and η'-region. The ω-signal occures due to its $\omega \to \pi^0\gamma$ decay where one soft photon is missing. The η' is seated on a large background. Figure 1.3.c) shows the η peak and Figure 1.3.d) the η' peak after kinematic fitting.

The results of the kinematic fit together with the additional cuts are given in table 1.4. The total number of accepted $\pi^+\pi^-\eta$ events is 79407.

run period	4C-fit	$\pi^+\pi^-\pi^0$	$\pi^+\pi^-\eta$	$\pi^+\pi^-\eta'$
Jun. '91	174329	85236	10413	313
Aug. '91	218382	113587	12571	323
Jun. '94	988331	512383	56423	1719
sum	1381042	711206	79407	2355

Table 1.4: Result of the kinematic fit

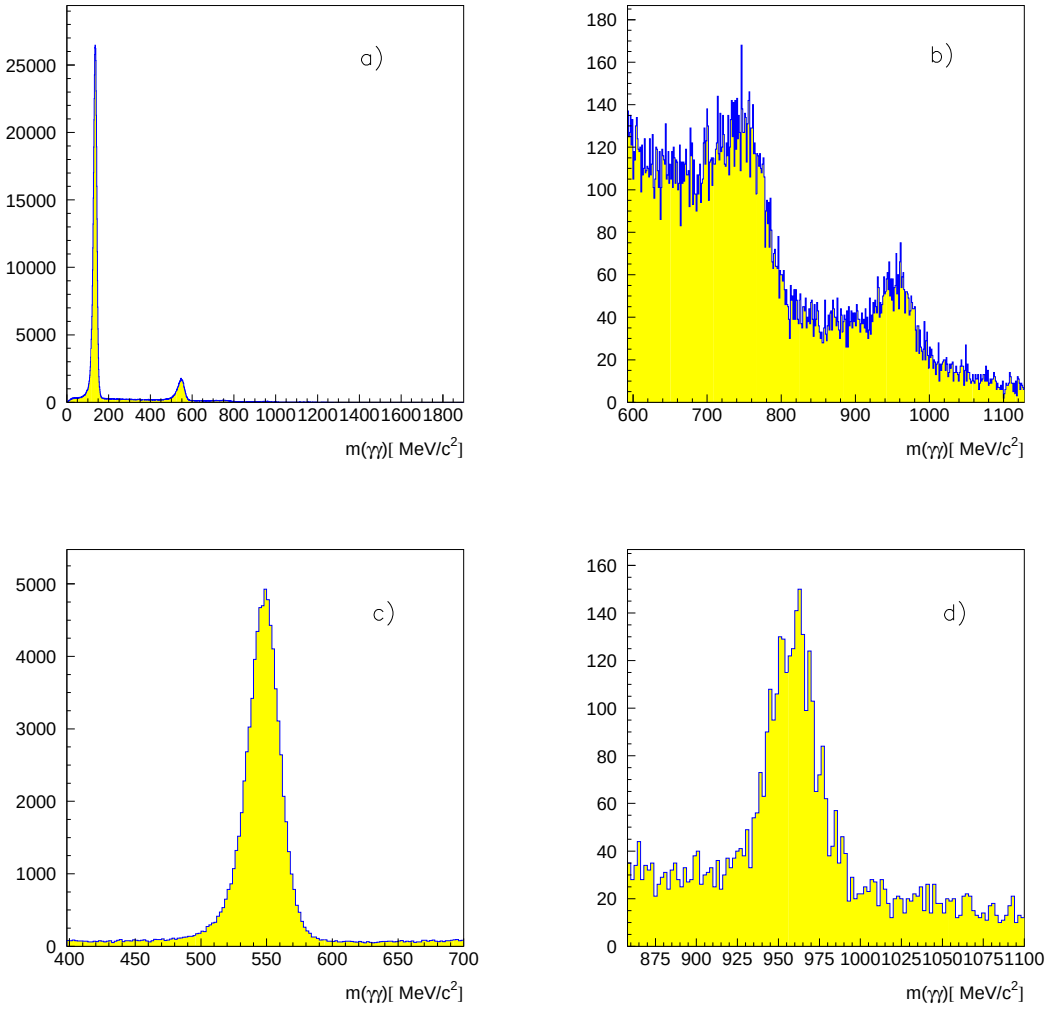

Figure 1.3: $\gamma\gamma$-invariant mass spectrum a), b) before, c), d) after KINFIT

1.3 $\pi^+\pi^-\eta$ – Dalitz plot

Figure 1.4 shows the Dalitz plot of the complete data set (79407 events). The main characteristics are the same as in $\pi^0\pi^0\eta$ [2] but with an additional ρ (not decaying into $\pi^0\pi^0$). Clearly visible are the ρ and the $f_0(980)$ in the $\pi^+\pi^-$ invariant mass and two cross like structures in the $\pi^\pm\eta$ invariant mass due to the $a_0(980)$ and the $a_2(1320)$.

The possible initial states from which annihilation can take place together with the resulting angular distributions are listed in table 2.1. Only initial states and intermediate resonances with angular momentum less or equal 2 are taken into account. This leaves the five possibilities $^1S_0$, $^3S_1$, $^1P_1$, $^3P_1$ and $^3P_2$.

The Dalitz plot is binned into 50×50 active cells each having a size of 52000 MeV$^2/c^4$ × 52000 MeV$^2/c^4$.

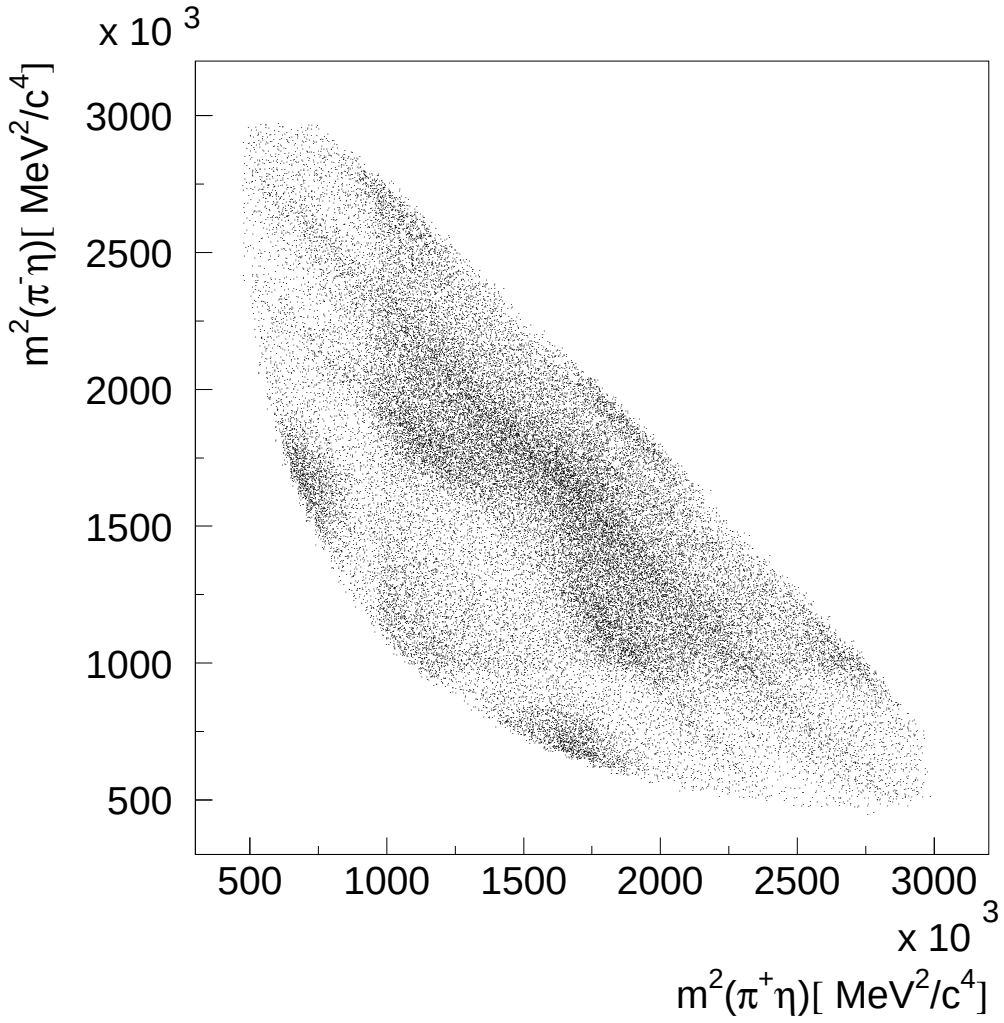

Figure 1.4: unbinned $\pi^+\pi^-\eta$-Dalitz plot

1.4 Acceptance correction

In order to check the acceptance 3.500.000 phase space distributed Monte-Carlo events were produce. Due to the fact that in June 1994 a new JDC was used we generate 1000000 events for the data from June '91 and August '91 (JDC 1) and 2500000 events for the June '94 data (JDC 2). These events were subjected to the same analysis chain as real data. To correct data, the MC distribution (see figure 1.5) is fitted using angular distribution functions. The fit is then normalized in a manner, that each cell provides a correction factor for each Dalitz plot entry. In the fits, bins not completely within the allowed phase space are not taken into account.

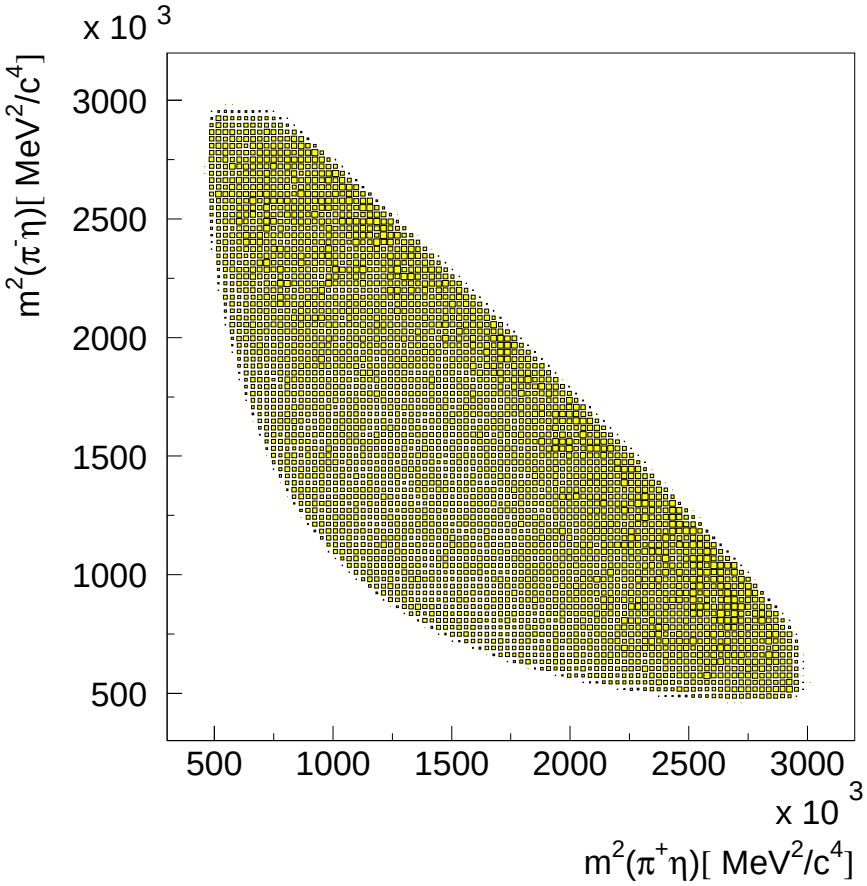

Figure 1.5: Acceptance distribution

Chapter 2

2.1 $\pi^+\pi^-\eta$ - Partial wave analysis

The partial wave analysis of the $\pi^+\pi^-\eta$ final state is based on the isobar model parametrized using the K-matrix formalism [3]. In order to achieve the dominant contributions to that final state a large number of fits has been done. First, we only take annihilation from the $^1S_0$- and the $^3S_1$-initial state into account. Then we add successively resonances from P-states.
The possible initial states from which annihilation can take place together with the resulting angular distributions are listed in table 2.1. Only initial states and intermediate resonances with angular momentum less or equal 2 are taken into account. This leaves the five possibilities $^1S_0$, $^3S_1$, $^1P_1$, $^3P_1$ and $^3P_2$.

$^{(2S+1)}L_J$	$I^G(J^{PC})$	l_m	l_d	state	$Z_{J^{PC},l_m,l_d}(\vec{P},\vec{Q})$	ang.dist.
$^1S_0$	$0^+(0^{-+})$	0	0	f_0, a_0	$\mathbb{1}$	1
		1	1	$\hat{\rho}$	$\vec{Q}\cdot\vec{P}$	$\cos^2\theta$
		2	2	f_2, a_2, a_2'	$(\vec{P}\cdot\vec{Q})^2 - \frac{1}{3} \mid \vec{Q} \mid^2 \mid \vec{P} \mid^2$	$(\cos^2\theta - \frac{1}{3})^2$
$^3S_1$	$1^+(1^{--})$	1	1	ρ, $\hat{\rho}$	$\vec{Q}\times\vec{P}$	$\sin^2\theta$
		2	2	a_2, a_2'	$(\vec{Q}\cdot\vec{P})(\vec{Q}\times\vec{P})$	$(\cos\theta\sin\theta)^2$
$^1P_1$	$1^+(1^{+-})$	1	0	a_0	$\vec{P}$	1
		0	1	ρ, $\hat{\rho}$	$\vec{Q}$	1
		1	2	a_2, a_2'	$\vec{Q}(\vec{P}\cdot\vec{Q}) - \frac{1}{3} \mid \vec{Q} \mid^2 \vec{P}$	$\cos^2\theta + \frac{1}{3}$
$^3P_1$	$0^+(1^{++})$	1	0	f_0, a_0	$\vec{P}$	1
		0	1	$\hat{\rho}$	$\vec{Q}$	1
		1	2	f_2, a_2, a_2'	$\vec{Q}(\vec{P}\cdot\vec{Q}) - \frac{1}{3} \mid \vec{Q} \mid^2 \vec{P}$	$\cos^2\theta + \frac{1}{3}$
$^3P_2$	$0^+(2^{++})$	1	2	f_2, a_2, a_2'	$\vec{Q}(\vec{P}\times\vec{Q})^T_s$	$\sin^2\theta$
		2	1	$\hat{\rho}$	$\vec{P}(\vec{Q}\times\vec{P})^T_s$	$\sin^2\theta$

Table 2.1: Initial and final angular momentum states and angular distributions for the $\pi^+\pi^-\eta$ final state.

Pol	m $[MeV/c^2]$	$\tilde{\Gamma}_{\pi\pi}$ $[MeV/c^2]$	$\tilde{\Gamma}_{K\bar{K}}$ $[MeV/c^2]$
1	855	774	0
2	1268	1311	72
3	1493	14	116
$c_{11} = c_{22} = 0, \quad c_{12} = 0.78$			

Table 2.2: K-matrix poles for $(\pi\pi)_S$-wave 1.

Pol	m $[MeV/c^2]$	$\tilde{\Gamma}_{\pi\pi}$ $[MeV/c^2]$	$\tilde{\Gamma}_{K\bar{K}}$ $[MeV/c^2]$
1	834	601	0
2	1218	648	12
3	1971	692	0
$c_{11} = c_{22} = 0, \quad c_{12} = 0.81$			

Table 2.3: K-matrix poles for $(\pi\pi)_S$-wave 2.

Pol	m $[MeV/c^2]$	$\tilde{\Gamma}_{\pi\pi}$ $[MeV/c^2]$	$\tilde{\Gamma}_{K\bar{K}}$ $[MeV/c^2]$
1	845.43	734.45	0
2	1206.5	67.42	237.1
3	1173.1	621.3	0
4	1548.1	254.5	0
$c_{11} = c_{22} = 0, \quad c_{12} = 0.988$			

Table 2.4: K-matrix poles for $(\pi\pi)_S$-wave 3.

Fits to the experimental distribution with different theoretical amplitudes are done using the χ^2 -method.
The main purpose of this work is to examine the $\pi^+\pi^-\eta$-final state but not to find a new description for the $(\pi\pi)_S$-wave. We try three different representations of the $(\pi\pi)_S$-wave which were derived in different analysis of the $3\pi^0$ and $2\pi\eta$ final states. These are

1. A 3-pole solution from the $3\pi^0$ final state [1]
2. A 3-pole solution from the $\pi^0\pi^0\eta$ final state [2]
3. A 4-pole solution from the $3\pi^0$ final state [1]

The poles of the 2×2 K-matrices are listed in table 2.2, 2.3, 2.4.

Since charged pions are no eigenstates to the C-operator, more initial states are allowed for resonances for $\pi^+\pi^-\eta$-final state than for $\pi^0\pi^0\eta$-final state. The allowed inital states for the used resonances are listed in table 2.1.

In a first step we try to figure out the best parametrisation of the $(\pi\pi)_S$-wave for the $\pi^+\pi^-\eta$ - final state. We take the following hypothesis (always with fixed $(\pi\pi)_S$-wave):

1. $(\pi\pi)_S$-wave, $a_0(980)$ and $a_2(1320)$ from $^1S_0$. $a_2(1320)$ and $\rho(770)$ from $^3S_1$ (masses and widths fixed)
2. hypo 1. with a additional $a_0(1450)$ from $^1S_0$.
3. hypo 2. but all masses and widths free (except $(\pi\pi)_S$-wave).
4. hypo 3. with a additonal $f_2(1275)$ from $^1S_0$ (fixed).
5. hypo 3. + ρ from $^1P_1$. $a_2(1320)$ from $^1P_1$, $^3P_1$ and $^3P_2$.
6. hypo 5. + $f_2(1275)$ from $^3P_1$ and $^3P_2$.
7. hypo 6. + $a_0(980)$ and $a_0(1450)$ from $^1P_1$ and $^3P_1$. $(\pi\pi)_S$-wave from $^3P_1$.

The χ^2/ndf of the fits is shown in table 2.5 and figure 2.1.

$(\pi\pi)_S$-wave	1	2	3
hypo 1	5.96	4.38	2.61
hypo 2	2.55	2.42	2.21
hypo 3	2.09	2.16	2.08
hypo 4	2.02	1.79	1.99
hypo 5	1.88	1.76	1.89
hypo 6	1.79	1.63	1.83
hypo 7	1.55	1.43	1.51

Table 2.5: χ^2/ndf of the used $(\pi\pi)_S$-wave for each fit

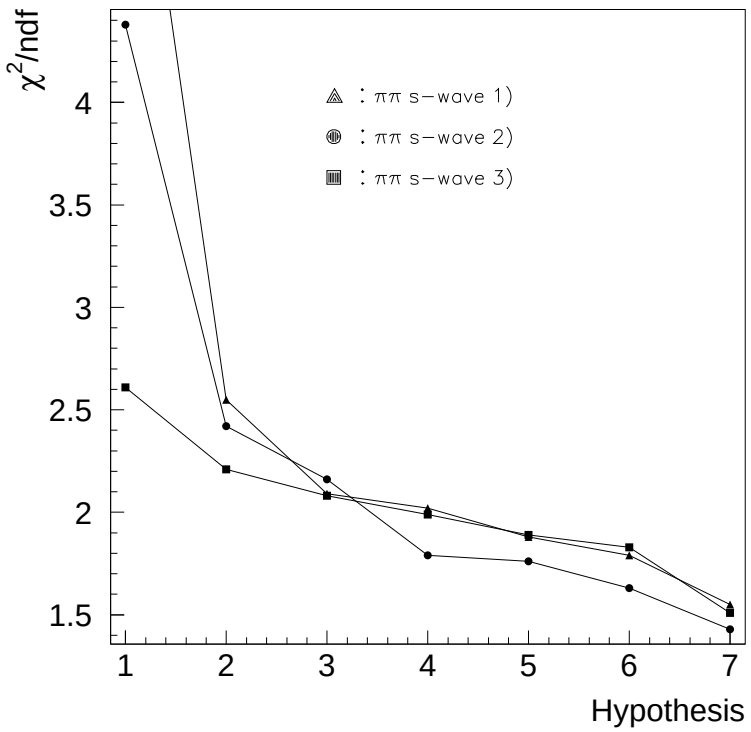

Figure 2.1: χ^2/ndf

Since $(\pi\pi)_S$-wave '2' is the best solution except for the first fits, where the 4-pole solution compensates the missing resonances better, we decide to take $(\pi\pi)_S$-wave 2) . Furthermore we add the $\hat{\rho}(1405)$ and the a_2'(1620). Then we start again with $^1S_0$ and $^3S_1$ initial states and include step by step one resonance. The $(\pi\pi)_S$-wave and the masses and widths of the $f_2(1275)$, the $\hat{\rho}(1405)$ and the a_2'(1620) are fixed, the other parameters are left free in the fit. In the following the general behaviour of the fits is outlined (see also table 2.6):

- The starting point of the analysis is fit 1, allowing only resonances from $^1S_0$ and $^3S_1$ with a $\chi^2 = 1434.9$.
- The necessity of of a P-wave contribution for ρ is checked with fit 2. The result is a decrease of χ^2 by $\Delta\chi^2/\text{ndf} = 99.7$ with $\chi^2 = 1335.3$.
- In fit 4,5 and 6 we tested the contributions of the a_0 and the f_0 from $^3P_1$. In fit 4 for the f_0, in fit 5 for the a_0 and in fit 6 for both. This leads to a difference in chisquare of $\Delta\chi^2 = 24.7$ with a $\chi^2 = 1310.5$
- In fit 7 the effect of an a_2' from $^3P_1$ was investigated.

- The next question was the necessity of a $f_2(1275)$. Fit 8 shows the change in χ^2. Since the contribution of the $f_2(1275)$ from ${}^1S_0$ is weak, we tried to leave out this initial state. The result shows fit 14.

- Fit 9 shows the result of allowing the ${}^1P_1$ initial state for the $a_2(1320)$. Earlier fits had shown that no essential contribution of the a_2 from the ${}^3P_1$ inital can be observed.

- In fit 10 the ρ-parametrization is changed from a Breit-Wigner to the resonance formula which will be presented in chapter 3. This improves the χ^2 by $\Delta\chi^2 = 82.2$.

- Table 2.8 shows that the branching ratios of the $\hat{\rho}(1405)$ and the $a_2(1620)$ from ${}^1S_0$ are really small. Due to this fact we tried the best fit (fit10) leaving out the $\hat{\rho}(1405)$ from ${}^1S_0$ (fit 11) and in a second step also the $a_2'(1620)$ from ${}^1S_0$ (fit 12). Fit 13 presents the result if we don't use $\hat{\rho}(1405)$ and $a_2'(1620)$ neither from ${}^1S_0$ nor from ${}^3P_1$.

The main results of our fits are:

- The $a_0(1450)$ is needed to describe the dips in the $a_0(980)$ bands.

- The fits show no clear evidence for a $f_2(1275)$ from ${}^1S_0$ and a weak contribution to the Dalitz plot from ${}^3P_1$

- $\hat{\rho}$ and a_2' show no clear structure in the Dalitz plot but lead to a better chisquare.

- The contributions from ${}^3P_2$ are negligible.

The final essential contributions to the Dalitz plot are listed in table 2.7, their branching ratios in table 2.8.

2.2 Branching ratio $\bar{p}p \to \rho\eta$

In order to determine the coherence parameter (see chapter 3: $\rho - \omega$ interference), the branching ratio $\bar{p}p \to \rho\eta$ is needed. So we analysed 822.000 minimum bias events of the june '94 data. From the number of annihilations, the fraction of antiprotons stopping in the liquid H_2 target (0.96 ± 0.02), the number of $\pi^+\pi^-\eta$ events (minimum bias), and the reconstruction efficiency, we find

$$\mathrm{BR}(\bar{p}p \to \rho\eta) = (42.0 \pm 2.9) \cdot 10^{-4}$$

fit	$a_0(^1S_0)$	$a_0(^3P_1)$	$f_0(^1S_0)$	$f_0(^3P_1)$	$a_2(^1S_0)$	$a_2(^3S_1)$	$a_2(^1P_1)$	$f_2(^1S_0)$	$f_2(^3P_1)$
1	✓	-	✓	-	✓	✓	-	-	-
2	✓	-	✓	-	✓	✓	-	-	-
3	✓	-	✓	-	✓	✓	-	-	-
4	✓	-	✓	✓	✓	✓	-	-	-
5	✓	✓	✓	-	✓	✓	-	-	-
6	✓	✓	✓	✓	✓	✓	-	-	-
7	✓	✓	✓	✓	✓	✓	-	-	-
8	✓	✓	✓	✓	✓	✓	-	✓	✓
9	✓	✓	✓	✓	✓	✓	✓	✓	✓
10	✓	✓	✓	✓	✓	✓	✓	✓	✓
11	✓	✓	✓	✓	✓	✓	✓	✓	✓
12	✓	✓	✓	✓	✓	✓	✓	-	✓
13	✓	✓	✓	✓	✓	✓	✓	✓	✓
14	✓	✓	✓	✓	✓	✓	✓	-	✓

fit	$\rho(^3S_1)$	$\rho(^1P_1)$	$a_2'(^1S_0)$	$a_2'(^3P_1)$	$\hat{\rho}(^1S_0)$	$\hat{\rho}(^3P_1)$	χ^2/ndf
1	✓	-	✓	-	✓	-	1506.5/972
2	✓	✓	✓	-	✓	-	1463.0/973
3	✓	✓	✓	-	✓	✓	1400.4/972
4	✓	✓	✓	-	✓	✓	1335.3/967
5	✓	✓	✓	-	✓	✓	1375.1/968
6	✓	✓	✓	-	✓	✓	1310.5/962
7	✓	✓	✓	✓	✓	✓	1280.5/958
8	✓	✓	✓	✓	✓	✓	1255.6/958
9	✓	✓	✓	✓	✓	✓	1225.7/954
10	✓	✓	✓	✓	✓	✓	1143.5/952
11	✓	✓	✓	✓	-	✓	1229.4/956
12	✓	✓	-	✓	-	✓	1269.8/958
13	✓	✓	-	-	-	-	1293.4/960
14	✓	✓	✓	✓	✓	✓	1200.7/954

Table 2.6: fit results

initial state	resonance	amplitude	phase [°]
$^1S_0$	$a_0(980)$	3.64 ± 0.54	0
	$a_0(1450)$	0.76 ± 0.30	219.5 ± 17.4
	f_0 (pole 1)	2.51 ± 0.73	97.9 ± 8.3
	f_0 (pole 2)	4.35 ± 0.38	175.7 ± 26.8
	f_0 (pole 3)	1.12 ± 0.68	93.5 ± 31.1
	$a_2(1320)$	15.99 ± 0.46	200.4 ± 6.2
	a_2'(1620)	3.42 ± 0.67	42.7 ± 9.2
	$f_2(1275)$	7.21 ± 0.23	168.7 ± 5.8
	$\hat{\rho}(1405)$	0.56 ± 0.13	107.9 ± 12.7
$^3S_1$	$\rho(770)$	9.78 ± 0.38	0
	$a_2(1320)$	1.32 ± 0.42	299.2 ± 37.6
$^1P_1$	$\rho(770)$	3.77 ± 0.28	0
	$a_2(1320)$	4.85 ± 0.64	6.2 ± 21.4
$^3P_1$	$a_0(980)$	2.48 ± 0.23	180
	$a_0(1450)$	2.18 ± 0.25	192.0 ± 10.6
	f_0 (pole 1)	2.38 ± 0.78	183.0 ± 20.2
	f_0 (pole 2)	3.51 ± 0.44	186.6 ± 7.1
	f_0 (pole 3)	2.13 ± 1.24	264.4 ± 28.1
	a_2'(1620)	4.36 ± 0.43	76.8 ± 14.1
	$f_2(1275)$	7.85 ± 1.07	85.8 ± 13.9
	$\hat{\rho}(1405)$	2.11 ± 0.24	283.0 ± 13.9

Table 2.7: final fit results

resonance	$^1S_0$	$^3S_1$	$^1P_1$	$^3P_1$
a_0	(20.2±6.0)%	-	-	(4.3±1.8)%
f_0	(18.9±6.6)%	-	-	(5.9±2.4)%
a_2	(15.4±1.2)%	(0.3±0.2)%	(4.5±1.9)%	-
f_2	(0.6±0.1)%	-	-	(1.2±0.3)%
ρ	-	(18.0±1.4)%	(6.1±0.9)%	-
a_2'	(0.6±0.3)%	-	-	(1.4±0.3)%
$\hat{\rho}$	(0.1±0.02)%	-	-	(2.5±0.6)%

Table 2.8: branching ratios for resonances fitted in the $\pi^+\pi^-\eta$ Dalitz plot

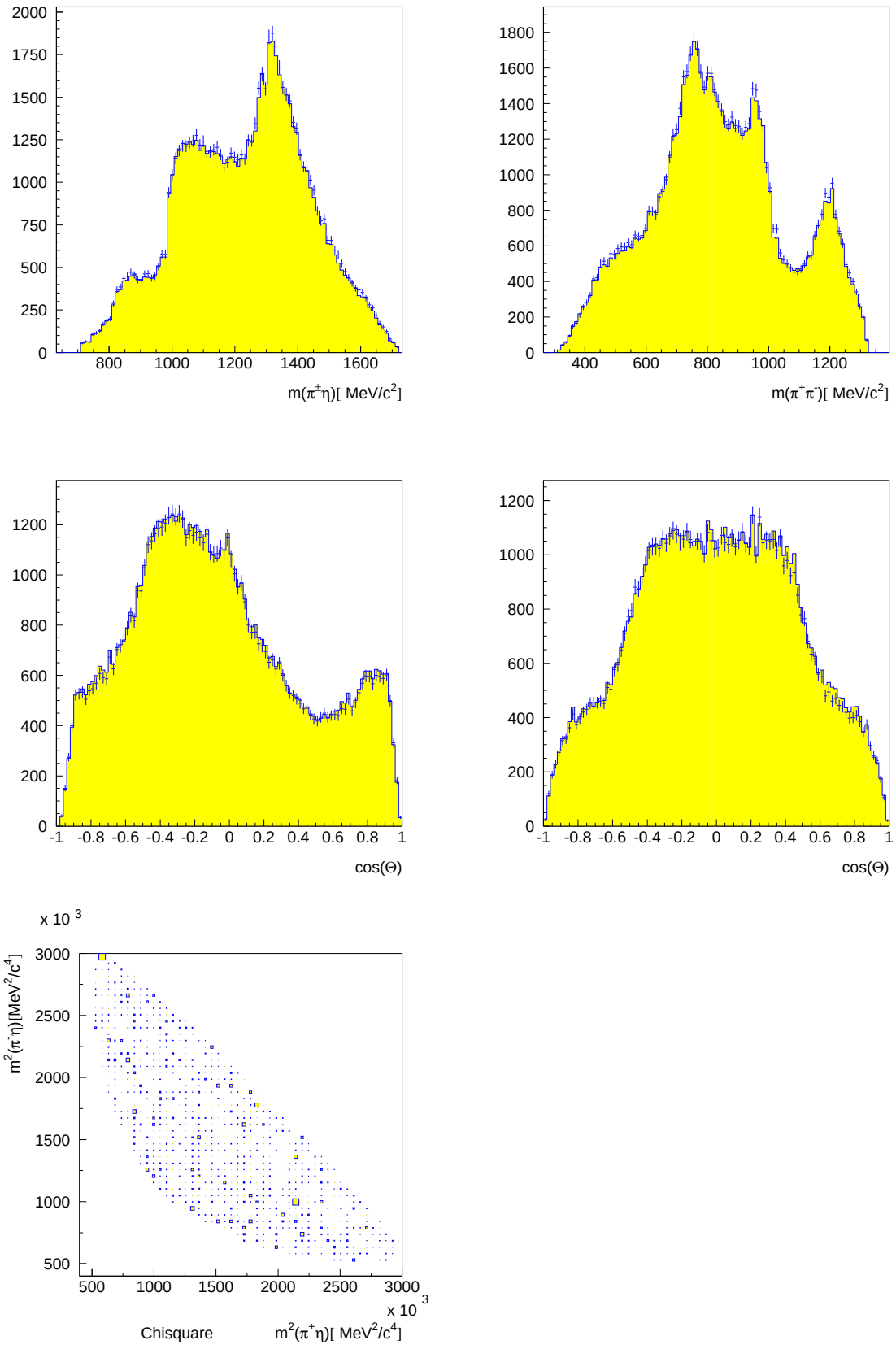

Figure 2.2: Results of the best fit. $\pi^{\pm}\eta$ projection, $\pi^{+}\pi^{-}$ projection, angular distribution in $\pi^{\pm}\eta$ and in $\pi^{+}\pi^{-}$, chisquare distribution in the Dalitz plot

Chapter 3

$\rho - \omega$ interference

3.1 $\rho - \omega$ interference in $\bar{p}p \to \pi^+\pi^-\eta$

Mixing of elementary particles with different quantum numbers may occur when a symmetry is broken, see e.g. in the $K^0 - \bar{K}^0$ system where CP is violated. In the case of $\rho - \omega$ - mixing isospin invariance is broken by electromagnetic interactions and/or the u,d quark mass difference . States with identical I_z but with different values of I are now allowed to mix. In the case of $\rho - \omega$ this effect is large due to the near degeneracy of the ρ and ω masses which increases the effects.
With exact SU(2) symmetry, isospin would be conserved and the physical states would be the orthonormal ones of the (I, I_z) basis: $\mid \rho^0 \rangle :=\mid 1,0 \rangle$ and $\mid \omega^0 \rangle :=\mid 0,0 \rangle$. In this basis the vector meson propagator would be diagonal. However the physical situation includes symmetry breaking effects and transitions with $\mid \Delta I \mid = 1$ may occur. The mass matrix is no longer diagonal in the isospin basis; the physical states no longer the isospin states. Instead, they result from a diagonalisation of the full mass matrix. The observed vector mesons ρ and ω are the linear combinations of the states $\mid \rho^0 \rangle$ and $\mid \omega^0 \rangle$ which diagonalize this matrix.
Since the mixing is observed to be small, we approximate the transformation between the two bases (to first order in ϵ) by:

$$\begin{aligned} \mid \rho \rangle &= \mid \rho^0 \rangle - \epsilon \mid \omega^0 \rangle \\ \mid \omega \rangle &= \mid \omega^0 \rangle + \epsilon \mid \rho^0 \rangle \end{aligned}$$

where ϵ is a small complex mixing parameter.

The large fraction 8.5% of the radiative decay $\omega \to \pi^0\gamma$ implies the presence of isospin violation and allows also for a sizable $\omega \to \pi^+\pi^-$ decay rate. Thus both, ρ and ω mesons, may contribute to the $\pi^+\pi^-$ final state; due to their different widths a characteristic interference pattern is observed which sheds light on the reaction mechanism.

The interference of ρ and ω mesons was studied for various reactions, both experimentally and theoretically. A recent discussion can be found in [4]. From this paper we take the $\pi^+\pi^-$ mass distribution in the form:

$$S = p \cdot q \left| \mathrm{BW}_\rho + \mathrm{BW}_\omega \cdot e^{i\alpha} \epsilon_{\mathrm{coh}} \cdot \frac{e^{i\varphi}}{m_\omega^2 - m_\rho^2 - i(m_\omega \Gamma_\omega - m_\rho \Gamma_\rho \frac{\rho(s)}{\rho(m_\rho^2)} \cdot B_1^\rho(q,q_\rho)^2)} \right|^2 \quad (3.1)$$

with

$$\mathrm{BW}_\alpha = \frac{D_1(p)\, A_\alpha\, m_\alpha\, \Gamma_\alpha / \rho(m_\alpha^2) \cdot B_1^\alpha(q,q_\alpha)}{m_\alpha^2 - s - i\, m_\alpha\, \Gamma_\alpha \frac{\rho(s)}{\rho(m_\alpha^2)} \cdot B_1^\alpha(q,q_\alpha)^2}$$

BW_α is a relativistic Breit-Wigner for resonance $\alpha = \rho, \omega$ with production amplitude A_α. The two vector mesons may be produced with a relative phase φ; we allow for partial incoherence of ρ and ω production by introducing a coherence factor ϵ_{coh}. B_1^α denotes a Blatt-Weisskopf factor describing the centrifugal barrier of the $\pi^+\pi^-$ interaction with l=1:

$$\begin{aligned}
B_1^\alpha(q,q_\alpha) &= \frac{D_1(q)}{D_1(q_\alpha)} \\
D_1(q) &= \frac{q}{p_r}\sqrt{\frac{2}{(\frac{q}{p_r})^2+1}} \qquad p_r = 197.3 \text{ MeV} \\
p &= \frac{\left[(M_{\bar{p}p}^2 - (\sqrt{s}+m_\eta)^2) \cdot (M_{\bar{p}p}^2 - (\sqrt{s}-m_\eta)^2)\right]^{1/2}}{2M_{\bar{p}p}} \\
q &= \frac{\left[s - 4m_{\pi^\pm}^2\right]^{1/2}}{2} \\
\rho(s) &= \frac{1}{\sqrt{s}}\sqrt{s - 4m_{\pi^\pm}^2}
\end{aligned}$$

Here we investigate $\rho - \omega$ interference in the reaction $\bar{p}p \to \pi^+\pi^-\eta$ for antiproton annihilation in liquid hydrogen. Particularly large interference phenomena can be expected since the branching ratio for $\bar{p}p \to \omega\eta$ is much larger $(1.51 \pm 0.12)\%$ [5], than for $\bar{p}p \to \rho\eta$ $(0.38 \pm 0.04)\%$. This may be contrasted to e^+e^- annihilation where vector meson dominance requires a $\rho : \omega$ production ratio of 9:1.

To compare the phase with a theoretical value, it can be calculated using the formula (181) from [4]:

$$\varphi = \arg\left(\frac{\Pi_{\rho\omega}}{m_\omega^2 - m_\rho^2 - i(m_\omega\Gamma_\omega - m_\rho\Gamma_\rho(m_\omega^2))}\right)$$

where $\Pi_{\rho\omega}$ is the $\rho - \omega$ mixing amplitude and is related to the branching ratios via

$$\frac{\Gamma(\omega \to \pi\pi)}{\Gamma(\rho \to \pi\pi)} = \left|\frac{\Pi_{\rho\omega}}{m_\omega^2 - m_\rho^2 - i(m_\omega\Gamma_\omega - m_\rho\Gamma_\rho(m_\omega^2))}\right|^2 = \epsilon^2$$

Using PDG values for masses and widths we get a theoretical value:

$$\Pi_{\rho\omega} = (3952 \pm 310)\ \mathrm{MeV}^2$$

The phase does not depend on $\Pi_{\rho\omega}$. It can be written in the form:

$$\tan\varphi = \frac{m_\omega \Gamma_\omega - m_\rho \Gamma_\rho(m_\omega^2)}{m_\omega^2 - m_\rho^2} \tag{3.2}$$

With PDG values $m_\omega = 781.94$ MeV, $m_\rho = 769.9$ MeV, $\Gamma_\omega = 8.43$ MeV and $\Gamma_\rho = 151.2$ MeV ($\Rightarrow \Gamma_\rho(m_\omega^2) = 152.8$ MeV) we obtain the phase:

$$\varphi = 80.45^\circ$$

The $\pi^+\pi^-$ invariant mass distribution of the final state $\pi^+\pi^-\eta$ and the fit using formula 3.1 is shown in figure 3.2. To simulate the limited detector resolution we calculate the convolution integral of the dynamical function with a Gaussian.
In order to find a good description for the background we fit a polynomal of second order to the $\pi^+\pi^-$ mass projection of our best fit but setting the ρ amplitude zero. This is done twice, once not including and once including the interference terms between ρ and the other resonances. The results are similar. Figure 3.1 shows the $\pi^+\pi^-$ mass projection with the ρ removed and our fit.

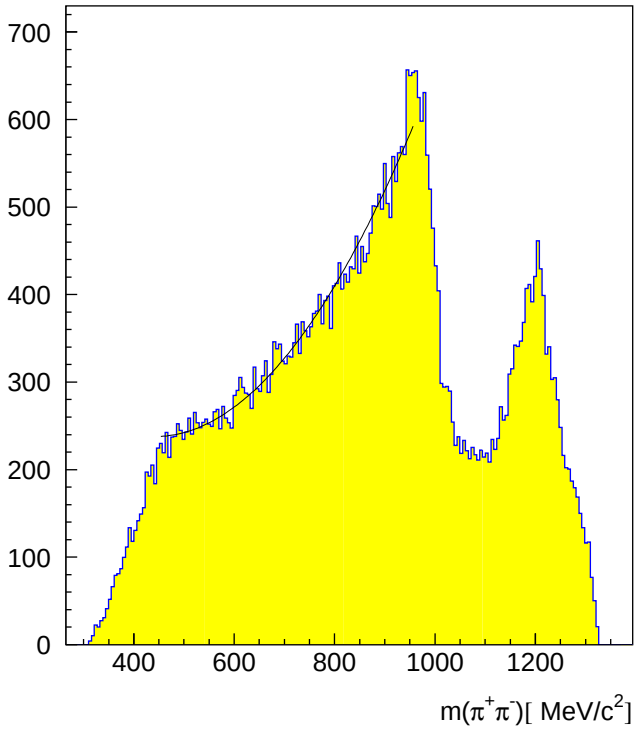

Figure 3.1: $\pi^+\pi^-$ mass projection excluding $\rho(770)$

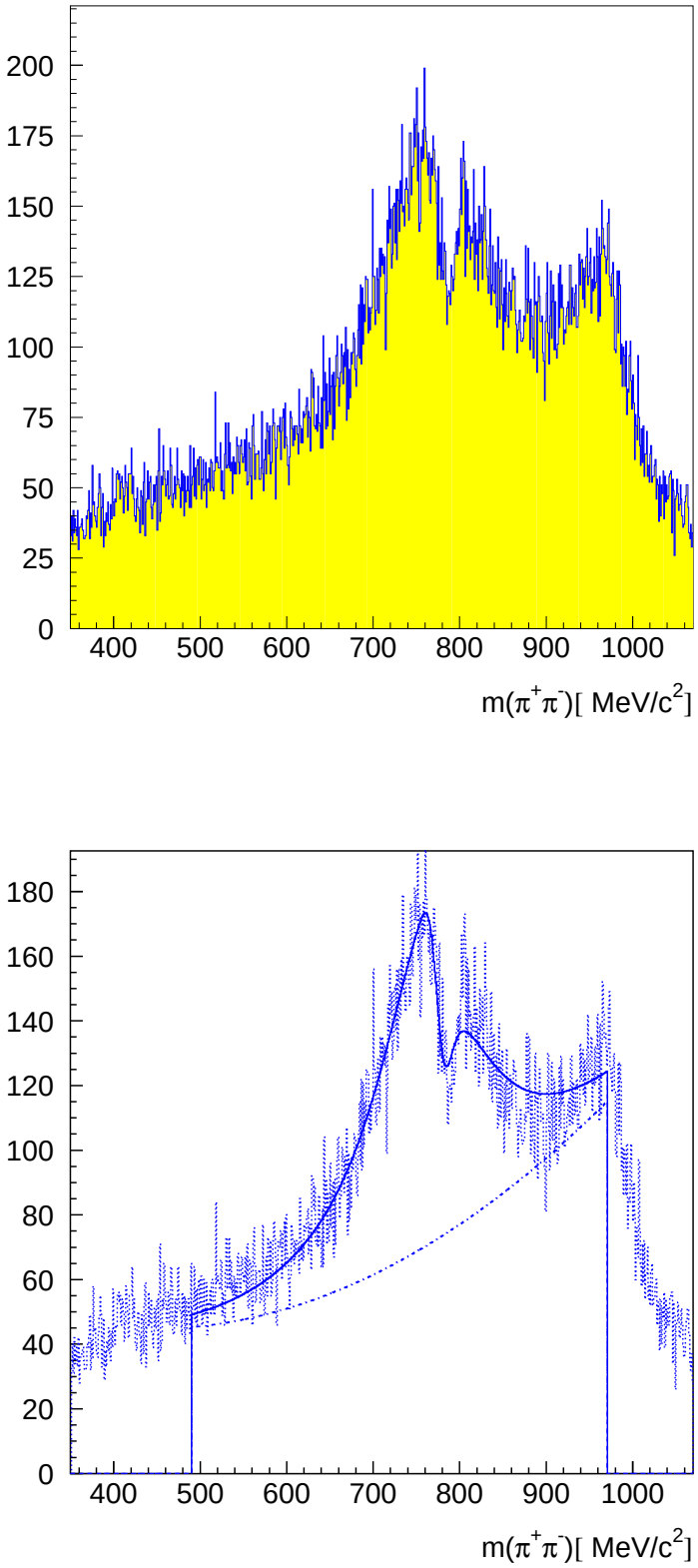

Figure 3.2: $\pi^+\pi^-$ invariant mass and fit using formula 3.1

We find $\epsilon_{\text{coh.}} = 1.17 \pm 0.15 \pm 0.13$. The first error contribution is statistical, the second represents the uncertainties in $\rho\eta$, $\omega\eta$ branching ratios, in the background estimate and in the (PDG) values of ρ and ω. The result is compatible with full coherence of the $\rho\eta$ and $\omega\eta$ production amplitudes. The ρ and ω masses and widths are fixed to the PDG values. We find a Gaussian width of $\sigma = 7.6 \pm 0.9$ MeV

Now we turn to an interpretation of the results on $\rho - \omega$ interference. In e^+e^- annihilation the $\rho - \omega$ interference angle is determined to $\varphi^{\text{exp}}_{e^+e^-} = (98 \pm 13.6)^\circ$ compatible with the theoretical value $\varphi^{\text{theory}}_{e^+e^-} = 100.5^\circ$ assuming that ρ and ω mesons are produced according to the quark decompositions $\rho, \omega = \frac{1}{\sqrt{2}}(\bar{u}u \mp \bar{d}d)$ with relative phase $\alpha_{\rho,\omega} = 0$. We find $\alpha^{\text{exp}}_{\bar{p}p} = (-5.4 \pm 1.8 \pm 3.9)^\circ$. Thus the relative phase between ρ and ω is nearly zero, the production amplitudes for $\bar{p}p \to \rho\eta$ and $\bar{p}p \to \omega\eta$ are relatively real, as predicted by quark models not taking initial or final-state-interaction into account.

3.2 $\rho - \omega$ interference in $\bar{p}p \to \pi^+\pi^-\pi^0$ and $\bar{p}p \to \pi^+\pi^-\omega$

Depending on the ratio of the branching ratios BR($\bar{p}p \to$xρ) and BR($\bar{p}p \to$xω) the $\rho - \omega$ - interference is more or less visible in other channels. Here we present two channels $\bar{p}p \to \pi^+\pi^-\pi^0$ and $\bar{p}p \to \pi^+\pi^-\omega$. For the first process the interference is only visible by an asymmetry of the right and left side of the ρ - signal. Since the ω exists only as a neutral particle this effect is not present for ρ^+ and ρ^-. Figure 3.3 shows the three ρ's compared with a relativistic Breit Wigner. Obviously we achieve a poor description for ρ^0

Due to the large branching ratio BR($\bar{p}p \to \omega\omega$) we expect a bigger effect for the second channel. This is confirmed in figure 3.4.

Branching ratios			
	x $= \eta$	x $= \pi^0$	x $= \omega$
BR($\bar{p}p \to$xρ)	$(3.85 \pm 0.13) \cdot 10^{-3}$	$(1.65 \pm 0.08) \cdot 10^{-2}$ [7]	$(2.38 \pm 0.11) \cdot 10^{-2}$
BR($\bar{p}p \to$xω)	$(1.51 \pm 0.12) \cdot 10^{-2}$ [5].	$(5.73 \pm 047) \cdot 10^{-3}$ [5]	$(3.32 \pm 0.34) \cdot 10^{-2}$ [5]
$\frac{\text{BR}(\bar{p}p \to x\rho)}{\text{BR}(\bar{p}p \to x\omega)}$	$\approx 1/4$	≈ 3	$\approx 3/4$

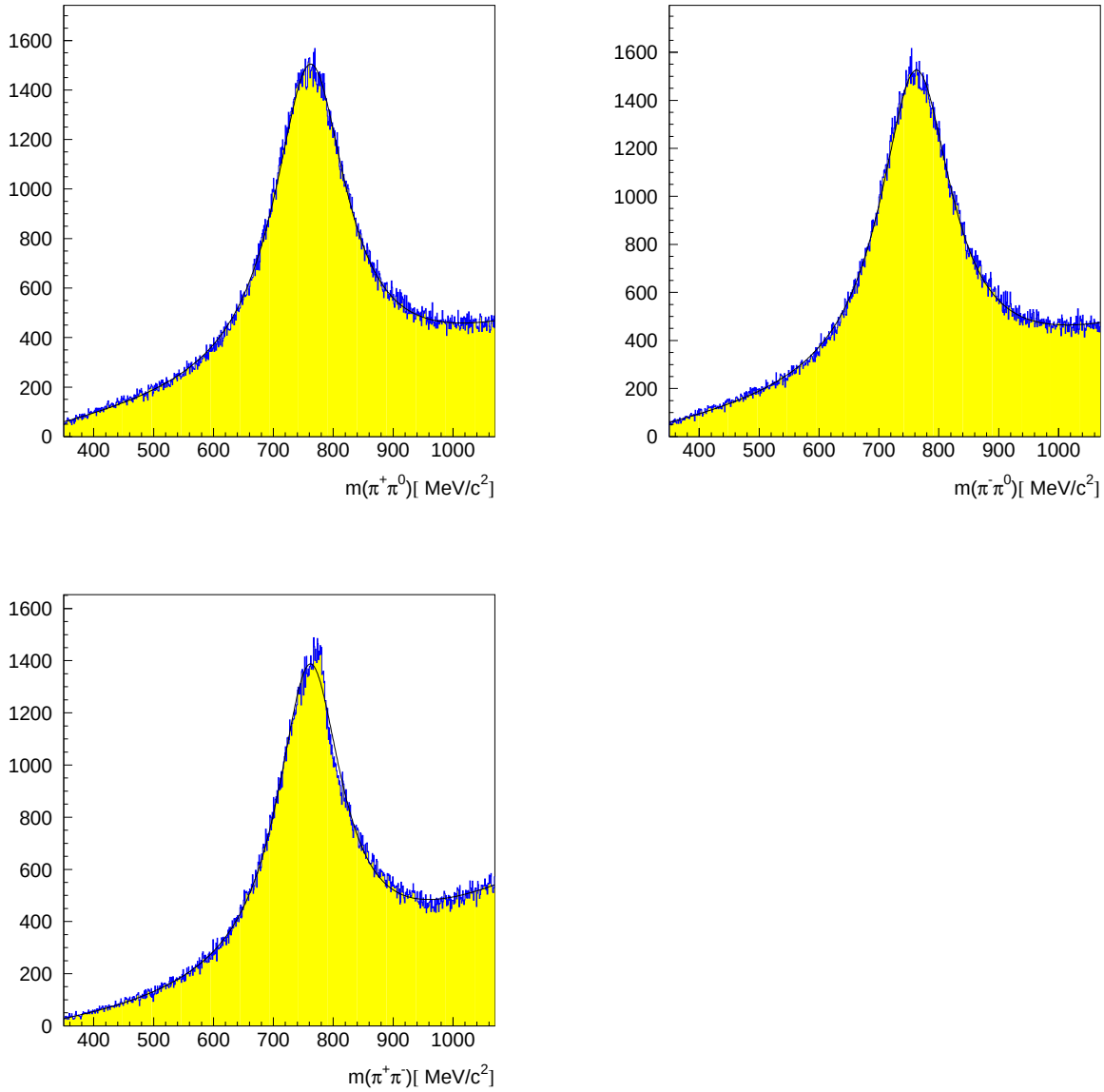

Figure 3.3: ρ^+, ρ^- and ρ^0 in $\pi^+\pi^-\pi^0$ final state

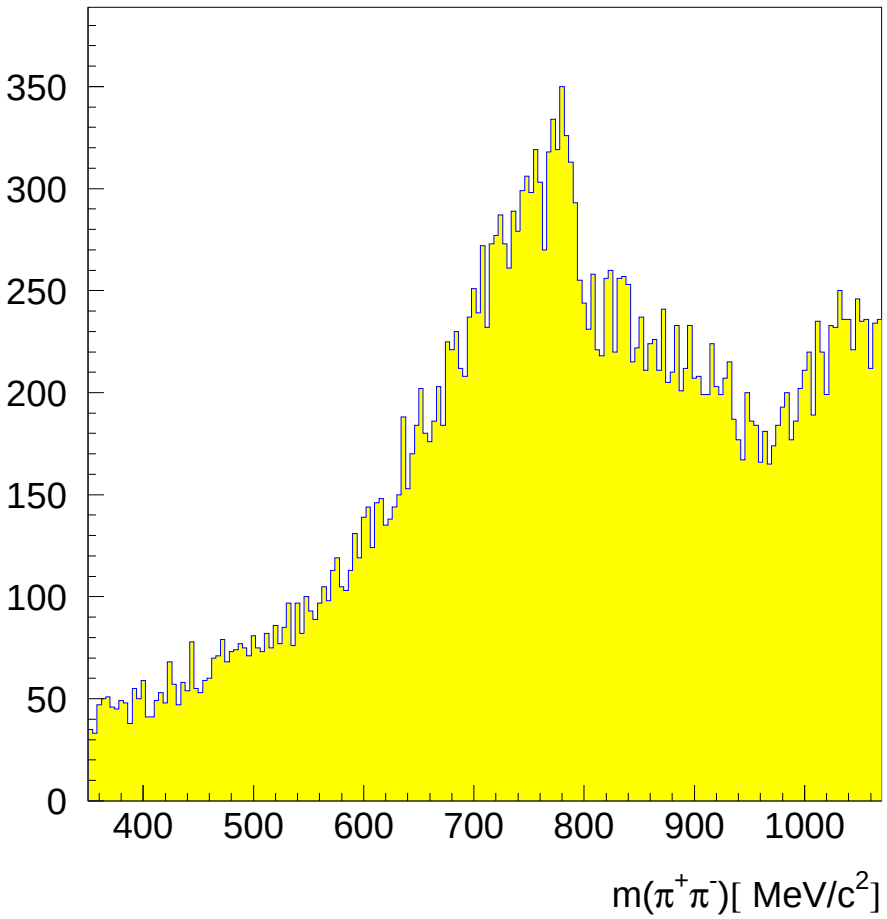

Figure 3.4: $\rho - \omega$-interference in $\bar{p}p \to \pi^+\pi^-\omega$

Bibliography

[1] C. Amsler et al.: Phys. Letters B 342, (1995) 433

[2] C. Amsler et al.: Phys. Letters B 333 (1994) 277

[3] S. U. Chung et al.: Ann. Physik 4 (1995) 404-430

[4] H.B. O'Connell et al., Rho-omega mixing, vector meson dominance and the pion form factor, University of Adelaide, Australia, ADP-95-1/T168, hep-ph/9501251

[5] C. Amsler et al.: Z. Phys. C 58, (1993) 175-189

[6] P. Weidenauer et al.: Z. Phys. C - Particles and Fields 47, 353-365 (1990)

[7] E. Klempt: Phys. Letters B 308 (1993) 179-185